Computational study of hypersonic flow past a CEV-like capsule on multiblock overlapping grids

By A. Lani, B. Sjögreen, H. C. Yee AND W. D. Henshaw

1. Motivation and objectives

In recent times, a growing interest of NASA and the whole aerospace community has risen on the prediction of the afterbody for space vehicles. As an example, great concern has been expressed by NASA for being able to better characterize the base flow heating and wake structure behind the Crew Exploration Vehicle (CEV), whose increased size, compared to previous similar capsules, implies higher Reynolds numbers and, consequently, a more important role of transition and turbulence in the aerothermodynamic design. To this end, conventional RANS models have proven not to be suitable for an accurate computational analysis, because of their deficiency in resolving unsteady wake dynamics in largely separated flows, due to an excessive amount of dissipation tending to smear out everything but the largest flow structures (Barnhardt & Candler 2008). A better compromise between cost and accuracy seems to be offered by Detached Eddy Simulation (DES) as advocated in Sinha *et al.* (2004), Barnhardt & Candler (2008), MacLean *et al.* (2009). However, a more reliable analysis by means of DNS (or alternatively LES) is still needed for better understanding this kind of flows and validating (or invalidating) the use of simplified models like DES.

The overarching goal of our project is precisely to gain deeper insight on turbulence in reentry high speed flows with strong shocks, including nonequilibrium effects induced by high temperature by means of our variable high-order finite difference solver for multiblock overlapping meshes (or simply overset) (Sjögreen *et al.* 2009), (Sjögreen & Yee 2009). The solver allows for catering suitable spatial discretization schemes on different regions (blocks) of the mesh to resolve relevant flow features with the appropriate degree of accuracy, and, moreover, already possesses DNS and LES capabilities for compressible flows (Hadjadj *et al.* 2010), (Yee *et al.* 2010).

The objective of the current investigation is a follow on work to Sjögreen & Yee (2009) to carry out additional validation on the overset grid implementation for a practical viscous perfect gas flows. The same flow past a Apollo-like CEV considered in Sjögreen & Yee (2009), Yee & Sjögreen (2006) but at a higher Reynolds number and on a finer overset viscous grid is considered here. This is a work-in-progress report of the first step of a multistep validation process. The results presented in this Technical Brief are preliminary. They are only meant to be used as an initial solution for comparison with future computations by more appropriate higher order schemes on the wake region, where shocklets or other turbulence-related unsteady flow phenomena might exist.

2. Numerical Scheme

In spite of the vast number of low-dissipative high-order schemes contained in ADPDIS3D, the variable high order finite difference solver for overset grids (Sjögreen & Yee 2009; Yee & Sjögreen 2006; Yee *et al.* 2008; Yee & Sjögreen 2009; Yee *et al.* 2010; Wang

$h[km]$	M_∞	$\rho_\infty[kg/m^3]$	$U_\infty[m/s]$	$\alpha[^o]$	$T_\infty[K]$	$T_w[K]$	$Re[10^6]$
35	16	0.0082	5000	0	237	553.3	1.76

TABLE 1. free-stream and wall conditions for the CEV simulation.

et al. 2010) used here, in the present preliminary study only the second-order Harten-Yee TVD scheme is considered for the discretization of the inviscid flux derivative (see Yee (1989) and references cited therein for details of the scheme). For the viscous flux derivatives the standard second-order central scheme is employed. Explicit second-order Runge-Kutta (RK2) is used in a time-accurate mode for the time discretization. Due to the explicit time-accurate computation, a very large number of iterations should be expected. With a sufficiently fine grid unsteady features of the flow field, if they exit, can be observed with this time-accurate approach. For the x inviscid flux derivatives $\mathbf{F}$, the numerical flux by the second-order Harten-Yee TVD scheme can be written (with all the y and z indices suppressed) as

$$\tilde{\mathbf{F}}_{j+\frac{1}{2}} = \frac{1}{2}\left(\mathbf{F}_j + \mathbf{F}_{j+1} + \mathbf{R}_{j+\frac{1}{2}}\mathbf{\Phi}_{j+\frac{1}{2}}\right), \tag{2.1}$$

where $\mathbf{R}$ is the matrix of right eigenvectors for the convective flux Jacobian and each component of $\mathbf{\Phi}_{j+\frac{1}{2}}$ denoted by $\phi^l_{j+\frac{1}{2}}$ with $l = N_s + 4$ is given by

$$\phi^l_{j+\frac{1}{2}} = \frac{1}{2}\psi\left(a^l_{j+\frac{1}{2}}\right)\left(g^l_j + g^l_{j+1}\right) - \psi\left(a^l_{j+\frac{1}{2}} + \gamma^l_{j+\frac{1}{2}}\right)\alpha^l_{j+\frac{1}{2}}, \tag{2.2}$$

with $\alpha^l_{j+\frac{1}{2}}$ being elements of $\mathbf{R}^{-1}_{j+\frac{1}{2}}(\mathbf{U}_{j+1} - \mathbf{U}_j)$ and

$$\gamma^l_{j+\frac{1}{2}} = \frac{1}{2}\psi\left(a^l_{j+\frac{1}{2}}\right)\begin{cases} (g^l_{j+1} - g^l_j)/\alpha^l_{j+\frac{1}{2}} & \alpha^l_{j+\frac{1}{2}} \neq 0 \\ 0 & \alpha^l_{j+\frac{1}{2}} = 0 \end{cases}, \tag{2.3}$$

where ψ is the entropy correction function defined in Harten (1984). All our computations have been run with $g^l_j = \texttt{minmod}\left(\alpha^l_{j-\frac{1}{2}}, \alpha^l_{j+\frac{1}{2}}\right)$.

3. Results

A CEV-like configuration in conditions (see Table 1) taken from Sinha *et al.* (2004) corresponding to the maximum Reynolds number point in the reentry trajectory of the FIRE II experiment is considered. The latter is still a commonly used source of inflight aerothermodynamic data for atmospheric reentry. The computations have been run in unsteady mode, assuming perfect non-reactive gas and without a turbulence model on a series of overset grids with growing complexity to progressively enhance the resolution of some relevant flow features. For sufficiently fine grids and low Reynolds number the simulation could be considered as a DNS computation. The present preliminary results use the same TVD scheme on all blocks.

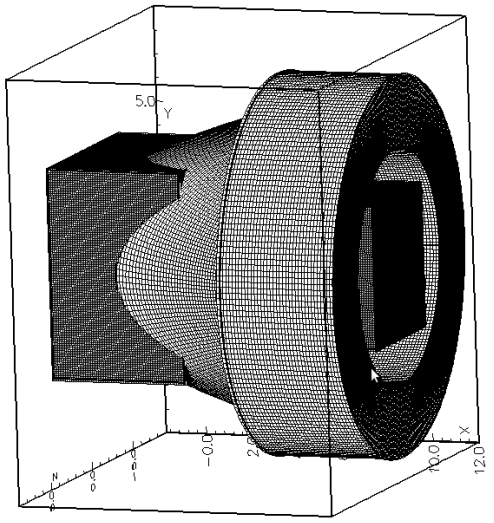

FIGURE 1. View on the internal blocks of the 9-block mesh used for the CEV computation.

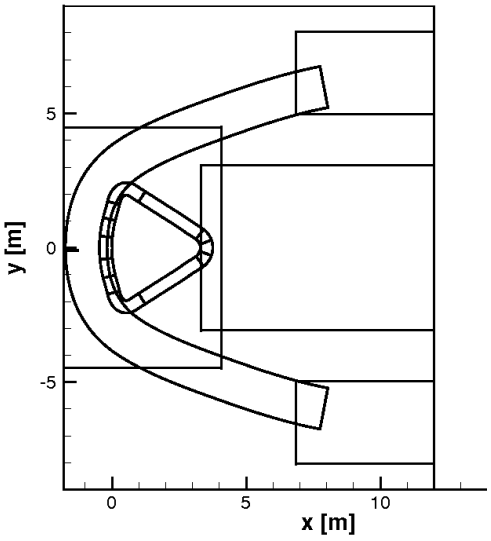

FIGURE 2. Block topology as seen in the xy (same as xz) plane for the 9-block mesh.

3.1. *Computational grids*

In order to ease the mesh generation process, the geometry of the CEV capsule base has been simplified compared to Barone's computation in Yee *et al.* (2008). Three overset meshes have been generated with Ogen (Henshaw 1998) for the unsteady simulation. The coarsest grid (6.9 M nodes) has a background and four blocks around the body (one surrounding the aft to better capture the separation and the originating shear layer), and it has been used to get a reasonably good estimation of the shock position. The intermediate grid (11.7M) has thinner cells near the boundary and one additional block to capture the wake. The finest grid adds two shock fitted blocks to completely enclose the bow shock and one block to smooth the transition between internal blocks and the much coarser background. A view of the last 9-block grid (26.2M nodes) is presented in Figure 1, where the background grid has been blanked out for visualization purposes. A snapshot depicting the block topology as seen on the x-y (or, similarly, on the x-z) plane is shown in Figure 2. In the last mesh design, particular care has been taken to allow for confining further refinements within the wake region, currently including 6.3M nodes. This topology also allows for larger overlap between blocks, as required by stencils for higher order discretizations which are planned to be used locally. In order to keep the computational cost affordable, for the moment, the size of the first cell on the wall has been set to 0.004 [m], i.e., about 300 times bigger than the value imposed by Barone in Yee *et al.* (2008). This mesh resolution is not fine enough to guarantee a reliable estimation of wall quantities such as heat fluxes and skin friction, which, therefore, will not be considered in this paper. Our focus will be on a phenomenological analysis of the whole flowfield and, in particular, of the unsteady wake.

3.2. *Parallel solution transfer algorithm*

A grid sequencing strategy has been used to transfer computed solutions from coarser to finer meshes. To this end, a generic parallel algorithm which reads and projects solutions from an overset mesh onto another, potentially with different block topology, has been

implemented. The interpolation is based on three meshes: (1) the donor mesh $\mathcal{M}^0$ with $\mathcal{N}_0$ blocks $\mathcal{M}^0_g$, (2) the new mesh $\mathcal{M}^1$ with N_1 blocks $\mathcal{M}^1_g$, (3) a coarse cartesian mesh $\mathcal{M}^C$, completely enclosing $\mathcal{M}^0$ (and therefore $\mathcal{M}^1$), subdivided into N_c^3 "boxes" $\mathcal{B}^C_i$ (with $N_c \leq 10$ for best performance and for keeping the associated data structure inexpensive). While looping over all blocks $\mathcal{M}^0_g$ each CPU:

- reads a part of the current block;
- classifies its points inside $\mathcal{M}^C$;
- stores states and square distances corresponding to N_p closest points from $\mathcal{M}^0_g$ (within the corresponding box $\mathcal{B}^C_i$) for each local node on $\mathcal{M}^1$;
- broadcasts the locally read part of $\mathcal{M}^0_g$ to all other CPUs;
- updates local interpolating data (states, square distances) on the base of input from other CPUs.

The actual interpolation of the solution array on the new mesh, $\mathbf{U}^1$, from the set of closest points data collected from the donor mesh is performed during a separate loop over blocks on the new mesh $\mathcal{M}^1_g$. Herein, a simple inverse-distance weighted average interpolation (Shepard's method) defined as $\mathbf{U}^1_i = \frac{\sum_{p=1}^{N_p} w_{p_{i,1}} \mathbf{U}^0_{p_{i,1}}}{\sum_{p=1}^{N_p} w_{p_{i,1}}}$ or more sophisticated approaches (for instance, based on lagrangian shape functions of locally constructed tetrahedra with positive volume) can be applied. Two of the main advantages of this algorithm are: (1) it speeds up the search for closest points by a factor $\leq N_c^3 \cdot N_{cpu}$ if compared to a serial non-constrained version; (2) it is truly parallel and, in particular, keeps scalability also in the memory requirements, because only mesh partitions of $\mathcal{M}^0$ and $\mathcal{M}^1$ are loaded in each process at all times, together with a full instance of $\mathcal{M}^C$, which is, however, extremely coarse and negligible for memory benchmarks. As an illustrative example, interpolating from a 11.7M onto a 26.2M nodes mesh currently takes about 12 minutes on 512 CPUs (including some sanity checks). Since the presence of shocks is ignored by the algorithm as is, problems can potentially occur if, in the vicinity of a shock, donor and current grid differ considerably. However, a more conservative treatment can be easily embedded within the actual interpolation phase during the last loop. For instance, a more suitable (and computationally expensive) approach could be applied where the pressure difference within the local set of closest points reaches a certain threshold.

3.3. *Parallel writing algorithm*

Given our need to frequently save increasingly bigger data files produced by our 3D unsteady simulations, a parallel algorithm has been developed to speed up the writing phase. The algorithm, here called multi-group (MG), combines inter and intra communication, i.e., global data exchange, in which all processes are involved, and local communication among a restricted number of processes belonging to the same group. The MG algorithm is a refinement on the concept described in Sjögreen *et al.* (2009) which uses one single group of writer processes. Each of the following steps is applied on each block of the overset mesh. Let N_{wr} be the number of concurrent writing processes and N_g a number of intervals (in global numbering) of the total number of points in k direction. N_g distinct MPI groups are defined to join processes which own data belonging to the same interval. The distributed data array $\mathbf{W}$ (solution and/or grid) is considered as composed by N_r data ranges to be written by each group g so that

$$\mathbf{W}^g_r = ([\forall c]\ [\forall i]\ [\forall j]\ [k_1, k_2])^g_r \ :\ \mathbf{W} = \bigcup_g \bigcup_r \mathbf{W}^g_r. \tag{3.1}$$

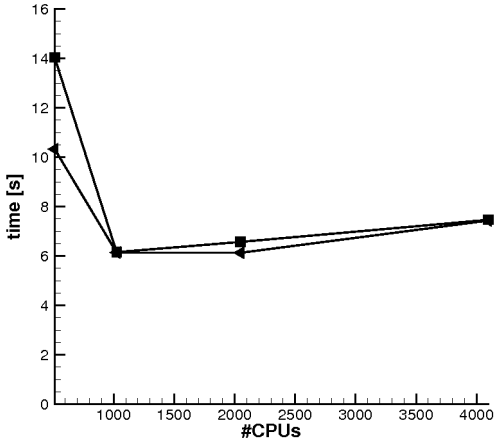

FIGURE 3. Performance of multi-group (left triangles) vs. single group (squares) algorithm assuming 100 writers and 100 stripes.

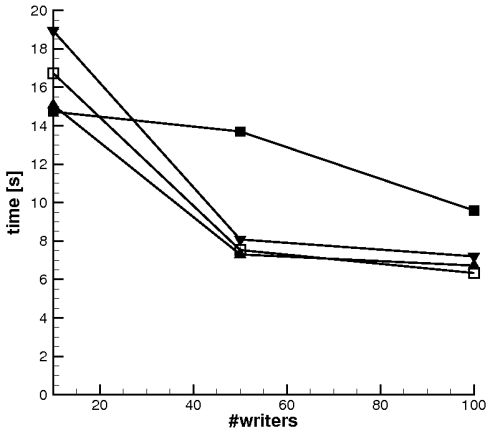

FIGURE 4. Performance of multi-group algorithm on 2 (squares), 10 (deltas), 50 (nabla), 100 (empty squares) stripes on 2048 CPUs.

While looping over all predefined ranges r, each CPU p sends its portion of data $(\mathbf{W}_r^g)_p$ to the corresponding group writer g where

$$(\mathbf{W}_r^g)_p = ([\forall c]\ [i_1, i_2]_p\ [j_1, j_2]_p\ [k_1, k_2]_p)_r^g\ :\ \mathbf{W}_r^g = \bigcup_p (\mathbf{W}_r^g)_p. \tag{3.2}$$

This is the key point of the algorithm: all data transfer from the computing processes to the group writing process is confined within each group, thereby reducing the cost of parallel communication. The designated writer CPU for each group first receives all range data and then writes them sequentially in binary format, concurrently with the other writers. For our benchmark the writing of a 5.6 Gb data file (corresponding to a single block mesh with 88M nodes) has been tested. Figure 3 shows the performance of MG and single group (not using intra-communication) algorithms on an increasing number of CPUs, on the NASA Lustre filesystem with 100 disks (stripes). Both algorithms show the peak performance around 1000 CPUs, but MG performs better up to 4096 CPUs. In this case, the maximum number of writing CPUs was set to 100 and by increasing this number the peak performance can be shifted higher. A similar effect was noticed in Sjögreen *et al.* (2009). In Figure 4 the effect of varying the number of filesystem stripes is investigated, while keeping constant the total number of CPUs (2048). Here, a clear advantage in using more than 10 stripes can be noticed, though the performance always improves by increasing the number of writers (at least up to the highest tested value, namely 100). In the best case, a 5.6 Gb file is written in about 6 seconds.

3.4. *Numerical results*

In the following section the flowfield evolution is examined during a time interval corresponding to 20 T_{flow} (being $T_{flow} = D/U_\infty$), starting from a randomly chosen instant t_0, at which the solution is fully developed and the bow shock already stabilized in its final position. Herein, three instantaneous solutions are analyzed at time t_0, $t_0 + 8\ T_{flow}$ and $t_0 + 20\ T_{flow}$. Figure 5 visualizes the cutting planes on which the solution will be shown at each selected time, namely x-z, x-y symmetry planes and three cross sections intersecting the wake corresponding to $x = 5.1[m]$, $x = 8.1[m]$ and $x = 11.9[m]$.

In Figures 6-14, the flowfield is depicted in terms of temperature isolines. In the snap-

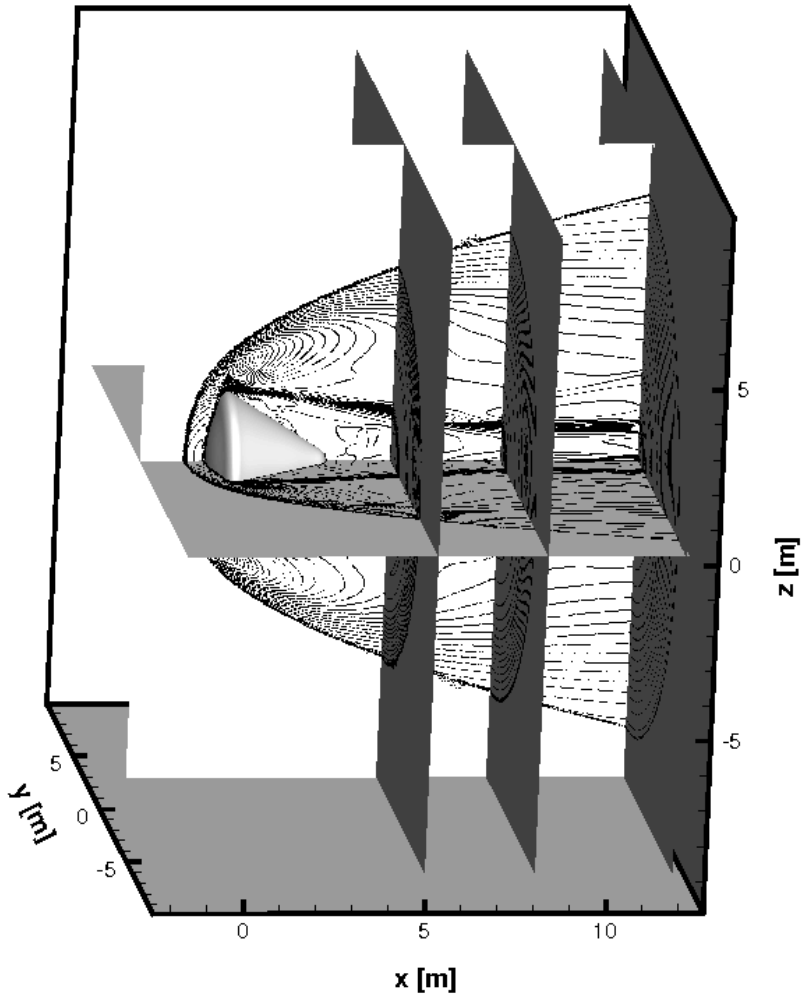

FIGURE 5. View on the cutting planes where the solution on CEV has been analyzed.

shots depicting x-y or x-z symmetry plane views, the main shock appears to be captured sharply even though some spurious wiggles are present in the junction between the two blocks enclosing it. The reason for this is currently under investigation. One possible explanation could be the non-conservative treatment of the inter-block lagrangian interpolation described in Sjögreen *et al.* (2009) or of the solution transfer algorithm in Section 3.2. Luckily, the problem does not seem to affect the flow in the region of interest, namely the afterbody and the wake. All the typical features of this kind of flow are well detected (see Sinha *et al.* (2004), Yee *et al.* (2008) for a comparison). After undergoing a severe compression through the bow shock, the flow heats up to about 12,600 K in the stagnation region. The strong expansion around the aft causes the temperature to drop considerably and the laminar boundary layer to separate at the beginning of the conical afterbody. A thick rake of shear layers forms, enclosing a large recirculation region characterized by fully 3D flow. The latter extends up to the neck region, about two capsule

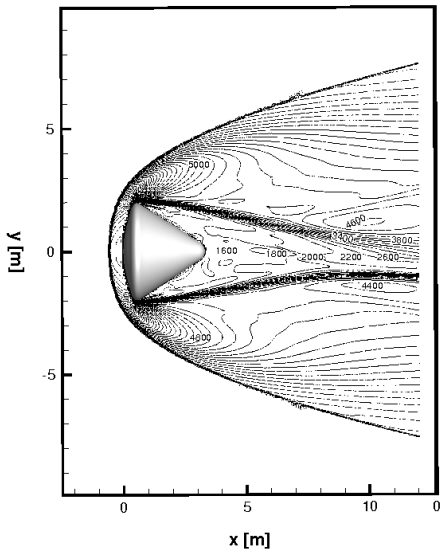

FIGURE 6. Temperature isolines for the CEV simulation on the x-y plane (snapshot at t_0).

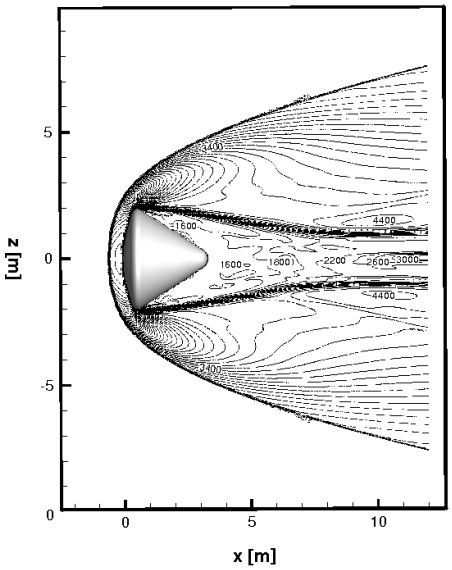

FIGURE 7. Temperature isolines for the CEV simulation on the x-z plane (snapshot at t_0).

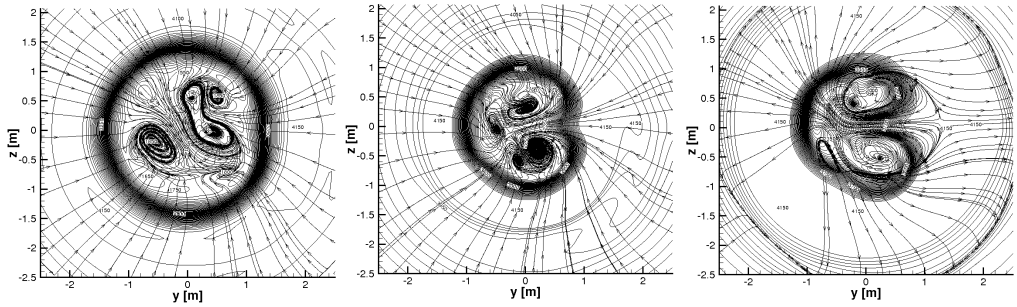

FIGURE 8. Temperature isolevels (K) and streamtraces on a wake crossplane y-z at $x = 5.1[m]$, $x = 8.1[m]$, $x = 11.9[m]$ at t_0.

diameters (D) further, where a weak recompression shock wave forces the flow to return parallel to the axis.

While the outer flow remains rather steady and symmetric at all locations, the initial steadiness and symmetry of the shear layers are lost after this point in the x-y plane (Figures 6, 9, 12), but not in the x-z plane (Figures 7, 10, 13). This is better visualized by the wake cross section plots. The first snapshots in Figures 8, 11 and 14 correspond to a cutting plane about one D before the neck and show almost perfectly circular shear sheets enclosing flow characterized by two large and two small counter-rotating vortices, tending to change in size and move around as time goes by.

The flow energizes along the streamwise direction leading the temperature to increase from about 1600 K near the base up to 3800 K in the vicinity of the neck. Here, the predicted temperature is much lower than the 9000 K found by DES in Sinha *et al.* (2004). This could be due to the lack of kinetic energy dissipation associated with the turbulent eddy viscosity, which is absent in our case. In the shear/shock interaction region

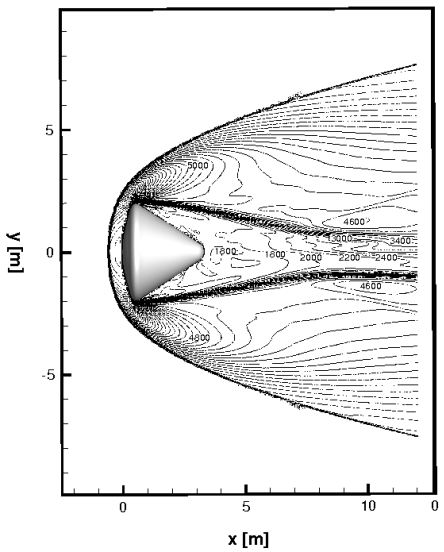

FIGURE 9. Temperature isolines for the CEV simulation on the x-y plane ($t_0 + 8\ T_{flow}$).

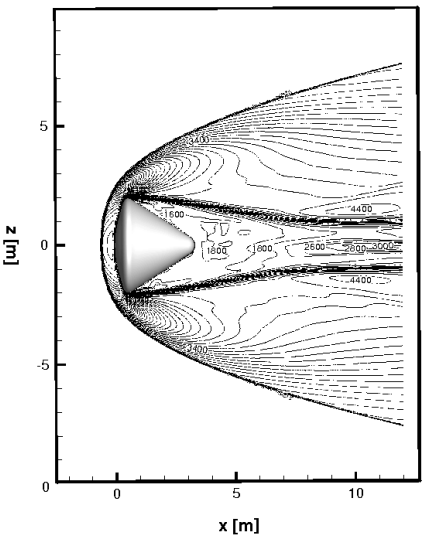

FIGURE 10. Temperature isolines for the CEV simulation on the x-z plane ($t_0 + 8\ T_{flow}$).

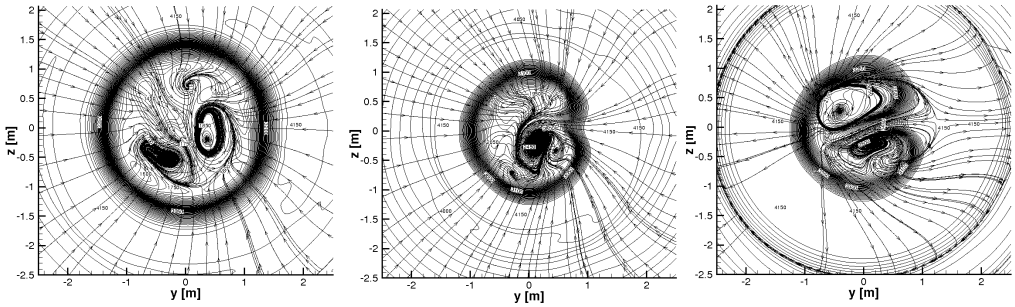

FIGURE 11. Temperature isolevels (K) and streamtraces on a wake crossplane y-z at $x = 5.1[m]$, $x = 8.1[m]$, $x = 11.9[m]$ at t_0.

(y-z plane mid-snapshots), the wake cross section assumes a kidney-like shape, due to the presence of two pairs of counter-rotating vortices, as clearly visible in Figures 8 and 14. In the outlet cross section (third pictures in y-z plots), the two main counter-rotating vortical structures tend to swing significantly with respect to each other. As a result of the vortex dynamics within the wake, the whole enclosing shear structure changes its shape significantly on the outlet plane, tending to expand and contract in the z direction.

A better characterization of the vortical structures in the recirculation region is given by the vorticity field. Figures 15, 16 and 17 show the z-component of the vorticity on the x-z plane at the three considered temporal instants. The vorticity distribution changes considerably within the time interval under investigation, but high values (lighter color) are always localized in the shear layers generated at the beginning of the conical afterbody, where the flow separates in the vicinity of and, especially, past the shock/shear interaction. The latter has the additional effect of inducing an anisotropic behavior on the vortical structures that tends to strongly align to the streamwise direction, consistent with what was pointed out in Sinha *et al.* (2004) using DES on a much coarser mesh

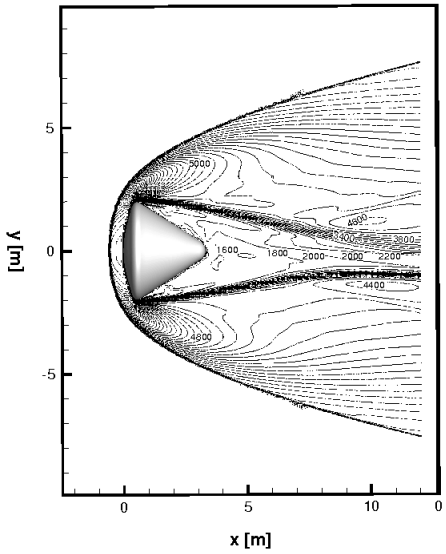

FIGURE 12. Temperature isolines for the CEV simulation on the x-y plane ($t_0 + 20\ T_{flow}$).

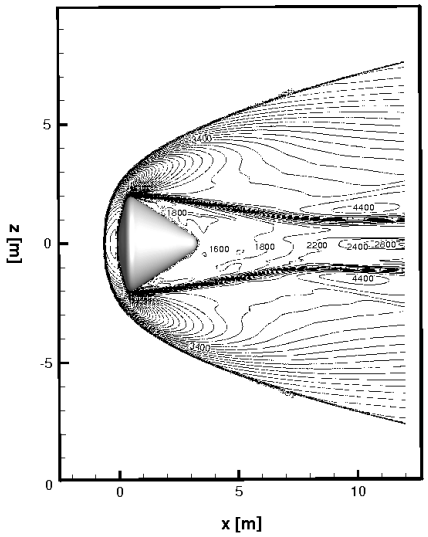

FIGURE 13. Temperature isolines for the CEV simulation on the x-z plane ($t_0 + 20\ T_{flow}$).

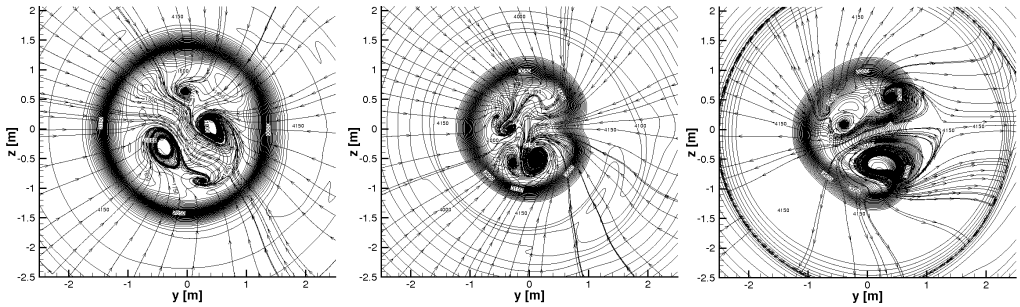

FIGURE 14. Temperature isolevels (K) and streamtraces on a wake crossplane y-z at $x = 5.1[m]$, $x = 8.1[m]$, $x = 11.9[m]$ at t_0.

within the wake region. If Figures 16 and 17 are compared, it can be noticed that it takes about 12 T_{flow} for the vorticity field to almost completely change sign, starting from about one diameter before the neck, while retaining an overall similar structure.

4. Conclusions and future plans

A preliminary study of the afterbody and wake structure of a space capsule, resembling NASA CEV vehicle under realistic flight conditions, has been presented. An unsteady simulation has been performed on a 9-block overset grid by assuming laminar non-reactive flow with the purpose of creating an input solution for a more detailed analysis with mixed higher order filter schemes as the main feature of ADPDIS3D. To this end, the overset grids framework is ideal for applying suitable high-order finite difference schemes where needed to reasonably complex cases, since it takes advantage of mesh topologies where relevant flow features are confined in separate blocks. The CEV simulation will be continued by applying appropriate fourth-order or higher schemes to the appropriate block

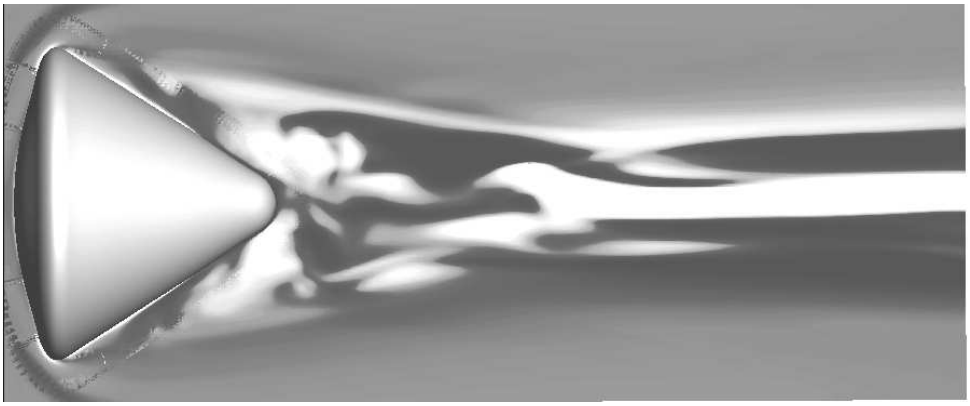

FIGURE 15. Instantaneous contours of vorticity ω_z on x-z plane at t_0.

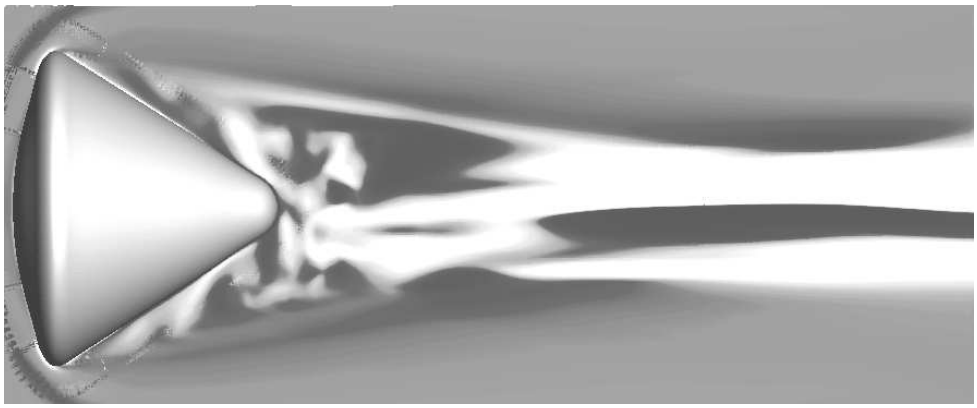

FIGURE 16. Instantaneous contours of vorticity ω_z on x-z plane at $t_0 + 8\ T_{flow}$.

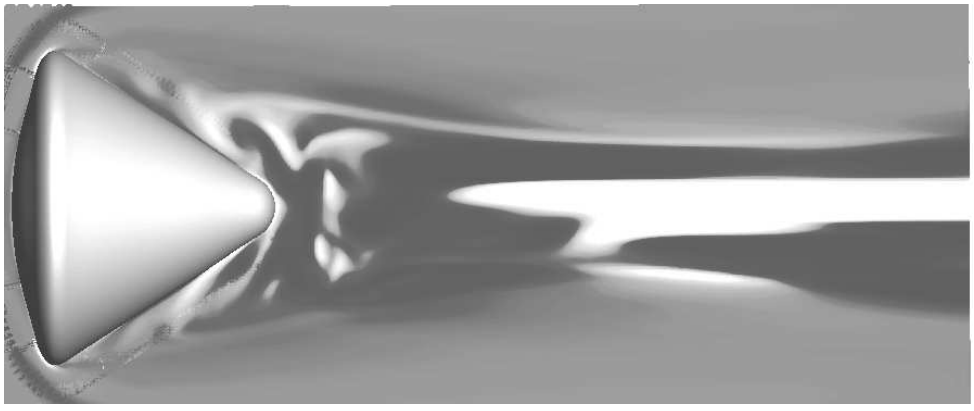

FIGURE 17. Instantaneous contours of vorticity ω_z on x-z plane at $t_0 + 20\ T_{flow}$.

grid in order to better resolve critical flow features such as the laminar boundary layer up to the capsule shoulder, the flow separation on the conical afterbody, the shock/shear interaction occurring in the neck region and the overall wake dynamics. Further mesh refinements are needed and should be feasible within the existing block topology.

Though the free-stream Reynolds number is not high enough to induce a fully turbulent wake, it should be sufficient to yield a transitional regime. With further development in LES subgrid scale model for high speed flow, ADPDIS3D is, in principle, ready for LES simulations. The ultimate goal will be to apply the developments on high-order schemes for nonequilibrium flows described in Wang *et al.* (2009) and Wang *et al.* (2010) to the same CEV configuration. This will provide deeper insight in the flow physics by taking into account the non-negligible effects of chemical dissociation/recombination induced by the high temperatures occurring in the shock layer and also significantly affecting the afterbody.

Acknowledgments

The authors wish to express their gratitude to A. Lazanoff and J. Chang of the Scientific Consultant Group, Code TN, NASA Ames for their help.

The support of the DOE/SciDAC SA grant DE-AI02-06ER25796 is acknowledged. Work by the second and fourth authors was performed under the auspices of the U.S. Department of Energy by the Lawrence Livermore National Laboratory under Contract DE-AC52-07NA27344. Part of the work by the third author was performed under the NASA Fundamental Aeronautics Hypersonic Program.

REFERENCES

Barnhardt, M. & Candler, G. 2008 Detached eddy simulation of the reentry-f flight experiment. 46th AIAA Aerospace Sciences Meeting, 7-10 January, Reno (Nevada), AIAA 2008-625.

Hadjadj, A., Yee, H. C. & Sjögreen, B. 2010 LES of temporally evolving mixing layers by high order filter schemes Submitted to *J. Comput. Phys.*

Harten, A. 1984 On a class of high resolution total variation stable finite difference schemes. *SIAM J. Num. Anal.* **2**, 1–23.

Henshaw, W. D. 1998 Ogen: An overlapping grid generator for Overture. Research Report UCRL-MA-132237. Lawrence Livermore National Laboratory.

MacLean, M., Mundy, E., Wadhams, T., Holden, M., Barnhardt, M. & Candler, G. 2009 Experimental and numerical study of laminar and turbulent base flow on spherical capsule. 47th AIAA Aerospace Sciences Meeting, 5-8 January, Orlando (Florida), AIAA 2009-783.

Sinha, K., Barnhardt, M. & Candler, G. 2004 Detached eddy simulation of hypersonic base flows with application to fire ii experiments. 38th AIAA Fluid Dynamics Conference and Exhibit, 28 June - 1 July, Portland (Oregon), AIAA 2004-2633-853.

Sjögreen, B. & Yee, H. C. 2009 Variable high order multiblock overlapping grid methods for mixed steady and unsteady multiscale viscous flow. *Comm. in Comput. Phys.* **5** (2-4), 730–744.

Sjögreen, B., Yee, H. C., Djomehri, J., Lazanoff, A. & Henshaw, W. D. 2009 Parallel performance of adpdis3d - a high order multiblock overlapping grid solver for hypersonic turbulence. Parallel CFD, Moffett Field (CA).

Wang, W., Shu, C. W., Yee, H. C. & Sjögreen, B. 2009 High-order well balanced schemes and applications to non-equilibrium flows. *J. Comput. Phys.* **228**, 6682–6702.

Wang, W., Yee, H. C., Sjögreen, B., Magin, T. & Shu, C. W. 2010 Construction

of low dissipative high-order well balanced filter schemes for non-equilibrium flows. *J. Comput. Phys.* .

Yee, H. & Sjögreen, B. 2009 High order filter methods for wide range of compressible flow speeds. In *Proceedings of ICOSAHOM 09, International Conference on Spectral and High Order Methods*. Trondheim, Norway.

Yee, H. C. 1989 A class of high-resolution explicit and implicit shock-capturing methods. In *VKI lecture series 1989-04*. NASA TM-101088.

Yee, H. C. & Sjögreen, B. 2006 Nonlinear filtering and limiting in high order methods for ideal and non-ideal mhd. *J. Sci. Comp.* **27**, 507–521.

Yee, H. C., Sjögreen, B. & Barone, M. 2008 High order numerical schemes for hypersonic flow simulations. In *VKI Lecture Series: Course on hypersonic entry and cruise vehicles*. Von Karman Institute for Fluid Dynamics, Stanford University, Palo Alto (CA).

Yee, H. C., Sjögreen, B. & Hadjadj, A. 2010 Comparative study of high order schemes for LES of temporally evolving mixing layers Extended version of the paper for the Proceedings of ASTRONUM-2010, June 13-18, 2010, San Diego, Calif; submitted to *J. Comp. & Fluids*.